Catalysis Science & Technology

PAPER

View Article Online
View Journal | View Issue

Cite this: *Catal. Sci. Technol.*, 2019, **9**, 2273

Improved photo-dechlorination at polar photocatalysts $K_3B_6O_{10}X$ (X = Cl, Br) by halogen atoms-modulated polarization†

Yang Zhang,[ab] Yufei Zhai,[c] Yang Yu,[b] Zhi Su,[a] Jiao Yin,[c] Chuanyi Wang [c] and Xiaoyun Fan *[b]

Received 22nd January 2019,
Accepted 8th April 2019

DOI: 10.1039/c9cy00148d

rsc.li/catalysis

The contamination of chlorophenols in water has been considered as an urgent environmental issue. In this study, two polar photocatalysts with a similar structure, $K_3B_6O_{10}Br$ (KBB) and $K_3B_6O_{10}Cl$ (KBC) were synthesized through a high temperature solid phase method and applied for the effective mineralization and removal of the chlorophenols. More than 92.0% of 2-chlorophenols can be fully degraded within 16 min under UV light irradiation, which is six times faster than the commercial P25 TiO_2 catalyst. The out-of-center distortions capability of the XK_6 octahedrons is greatly influenced by X (X = Cl and Br) atoms. The magnitude of the out-of-center distortion of KBC and KBB were 0.137 and 0.027, respectively. A better photocatalytic activity performance was therefore observed for KBC due to its higher spontaneous polarization ability and facile charge separation process. Kelvin probe force microscopy (KPFM) experiments further proved KBC has a larger surface potential change before and after the light irradiation. Reactive species capture experiments confirmed the role of radicals in the order of $^{\bullet}O_2^-$ > e^- > h^+ > $^{\bullet}OH$.

Introduction

Chlorophenols (CPs) are widely used in petrochemicals, insecticides, pharmaceuticals, synthetic dyes, wood preservatives and other industrial processes.[1,2] Effluents from petroleum refining, soil residual pesticides and metabolites of complex chlorinated hydrocarbons, once released into the environment, would seriously deteriorate environmental quality.[3,4] Various approaches, including chemical oxidation, biological and physical methods, have been developed for treating halogenated organic contaminant containing wastewater and groundwater.[5,6] However, the actual application of currently reported techniques is mainly limited by their high cost, low efficiency and potential risk of effluent.[6] A more cost-effective and efficient method to mineralize toxic CPs in water into harmless products is therefore crucially needed.

Photocatalysis as one typical advanced oxidation process has been considered as a promising method for the degradation and mineralization of CPs.[7–9] By now, numerous catalyst materials such as TiO_2,[10,11] ZnO,[12,13] Ag_3PO_4,[14,15] carbonitride ($g\text{-}C_3N_4$)[16,17] and WO_3,[18,19] have been reportedly applied for the photocatalytic degradation of CPs in water. The low photocatalytic efficiency is still a main obstacle for their actual application.[20] It is well known that photo-generated carriers recombine in a very short time before reaching the surface, so that photocatalytic reaction is highly dependent on the efficient separation of photo-generated electrons and holes which will greatly affect the transfer of the charges from the bulk to the surface active sites.[21]

Recently, photocatalysts with built-in electric field are proposed to promote the separation of photo-generated carriers which can drive the photo-induced electrons and holes to the opposite direction, so that the photo-generated charge carriers can be effectively separated and therefore the photocatalytic activity could be highly improved.[22–26] Much effort has been made to search for polar materials, such as, constructing of non-centrosymmetric by an asymmetrical π-conjugated plane of a borate material;[27] obtaining the asymmetric building units by controlling the cations to produce the second-order Jahn–Teller distortions;[28,29] and incorporating of the alkali metal cations into the borate systems to generate the polarized structures.[30] However, few studies had been reported to introduce halogen atoms into a borate motif to produce a more diversified structure. Therefore, we

[a] *College of Chemistry and Chemical Engineering, Xinjiang Normal University, Urumqi, 830054 Xinjiang, China*
[b] *School of Environment and Guangdong Key Laboratory of Environmental Pollution and Health, Jinan University, Guangzhou 510632, China. E-mail: xyfan@jnu.edu.cn*
[c] *Laboratory of Environmental Sciences and Technology, Xinjiang Technical Institute of Physics & Chemistry, and Key Laboratory of Functional Materials and Devices for Special Environments, Chinese Academy of Sciences, Urumqi 830011, China*

† Electronic supplementary information (ESI) available. See DOI: 10.1039/c9cy00148d

expected to use this approach to design and development of a new polar material.

In this study, two isomer non-centrosymmetric materials $K_3B_6O_{10}Br$ (KBB) and $K_3B_6O_{10}Cl$ (KBC) with built-in electric field were developed by incorporating the alkali cations and halogen atoms into the borate systems. The influence of halogen atoms on the different materials were investigated by the degradation of CPs, consisting of 2-chlorophenol (2-CP), 2,4-dichlorophenol (2,4-DCP), and 2,4,6-trichlorophenol (2,4,6-TCP) under UV light irradiation ($\lambda >$ 200 nm). The result showed that KBC material with higher distortion ability performed a larger surface polarization and higher degradation efficiency, after 16 min illumination, the dechlorination efficiency was approximately 92.2% for KBB and 97.9% for KBC. It is understood that this is the first time to report that the effect of different halide atoms on the structure and properties of polar $K_3B_6O_{10}X$ (X = Cl, Br) borate crystal materials as the photocatalysts for the dechlorination of CPs.

Experimental

Materials

K_2CO_3, H_3BO_3, KBr, KCl, KI, *tert*-butyl alcohol (TBA) were purchased from Tianjin Chemicals Co. Ltd. $AgNO_3$ was purchased from Shanghai Shanpu Chemical Reagent Co. Ltd. 2-CP, 2,4-DCP, 2,4,6-TCP, 5,5-dimethyl-1-pyrroline *N*-oxide (DMPO), 2,2,6,6-tetramethylpiperidine-1-oxyl (TEMPO), *p*-benzoquinone (*p*-BQ), methanol (chromatographic grade) and Nafion perfluorinated resin solution were obtained from Sigma-Aldrich Inc. Ultra-pure water was used in the preparation of all aqueous solutions, and all chemicals can be used directly without further purification.

Synthesis of the photocatalysts

The $K_3B_6O_{10}X$ (X= Cl, Br) powders were synthesized by the high temperature solid phase method. K_2CO_3, H_3BO_3, and KBr with stoichiometric ratio were grounded in an agate mortar and heated at 450 °C for 3 h, followed by keeping at 750 °C for 6 h for the final synthesis of KBB powder. KBC powder was synthesized in a similar method except for finally heating at 730 °C. Sufficient grinding during the constant temperature process makes the reaction more complete.

Characterization of samples

The structure and properties of the samples were investigated by X-ray diffraction (XRD), scanning electron microscopy (SEM), Fourier transform infrared spectroscopy (FTIR), UV-vis diffuse reflectance spectroscopy (DRS), high performance liquid chromatography (HPLC), Brunner–Emmet–Teller (BET), photoelectron chemistry (PEC), photoluminescence (PL) spectra, atomic force microscopy (AFM) combined with Kelvin probe force microscopy (KPFM) measurements, electron spin resonance (ESR), Second harmonic generation (SHG) tests and liquid chromatography-mass spectrometry (LC-MS). Photocatalytic activity measurements for KBX were conducted at room temperature. The specific details are described in the ESI.†

Photoelectron chemical (PEC) activities

A standard three-electrode cell with a working electrode (KBX electrode), a platinum plate as the counter electrode, and a standard calomel electrode (SCE) as a reference electrode were used in the photoelectron chemical activities which were measured at 0 V on an electrochemical system (CHI660E). The KBX solid power was dispersed in ethanol/Nafion solution which was dropped onto ITO glasses (1 × 1 cm), followed by air-drying. The photoelectric experiments were performed in a 50 mL quartz cylinder reactor by the removal of CPs (50 mg L^{-1}) in the solution of Na_2SO_4 (0.1 mol L^{-1}) which was placed in front of a 300 W xenon lamp (Perfect Light Company, Beijing, China).

KPFM measurements

Kelvin probe force microscopy (KPFM) measurements were performed at room temperature by Bruker Multimode 8 equipped with an atomic force microscope. KPFM measurements were recorded on a conductive Pt/Ir coated AFM tip (2.8 N m^{-1}) with a scan rate of 1 Hz, an AC mode scan size of 1 μm × 1 μm, and a resonant frequency of 75 kHz to obtain the topography in tapping mode. For the KPFM experiment, KBX dispersed in water and coated on the surface of a pre-cleaned ITO conductive glass to form a film, which would be dried in an oven at 100 °C for 6 h.

Detection of reactive species by electron spin resonance (ESR)

The spin strapping experiments were carried out using DMPO and TEMPO through electron spin resonance (ESR) measurements for the detection of active species $^{\bullet}O_2^-$, $^{\bullet}OH$ and e^-, respectively. In the typical measurement, a 10 mg sample was dispersed in 500 μL of methanol/H_2O that had been sparged with oxygen for 30 min, and then a 20 μL DMPO/TEMPO solution was added. The mixture was irradiated with a 300 W xenon lamp at regular intervals and then analyzed by ESR.

Results and discussion

Structure and physical properties of samples

The XRD patterns of two materials are presented in Fig. 1(a) and (c). It can be clearly seen that the two materials show a similar pattern except for the intensity is inconsistent. The crystal structures of KBB and KBC belong to nonconcentric symmetric triangular and rhombohedral space group $R3m$[31,32] with a three-dimensional network consisting of K, B, O atoms and X (X = Br, Cl) atoms (Fig. 1(b) and (d)), respectively. The coordination spheres of K atoms and X atoms are described in Fig. S1(a) and (b).† Three BO_4 tetrahedrons are connected by corner sharing of O atoms, while

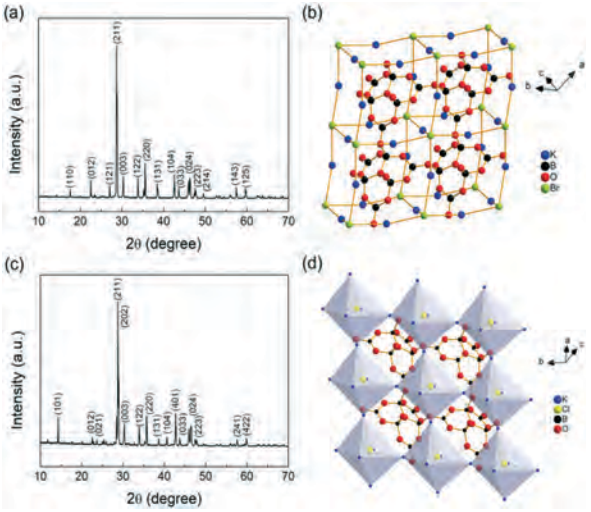

Fig. 1 (a) and (c) XRD pattern and (b) and (d) the crystal structure with the perovskite-related structure for KBB and KBC, respectively.

three BO_3 triangles are interconnected to form a compact hexaborate B_6O_{13} unit (Fig. S1(c)†), each B_6O_{13} unit and $[XK_6]$ X-centered octahedral are connected through vertex sharing to create a distorted perovskite-related framework.[32] The as-prepared samples show a bulk shape as shown in the SEM images (Fig. S2(a) and (c)†). The element constitution of the synthesized target samples was determined by EDX measurements (Fig. S2(b) and (d)†), which confirms that the existence of K, B, O and Br or Cl, respectively. The FTIR spectrum of KBB and KBC were shown in Fig. S3 and Table S1.† The peaks at 1301–1307, 1169–1173 and 969–974 cm^{-1} are attributed to the asymmetric stretching vibration of the BO_3 and BO_4 groups, respectively. While, for the symmetric stretching vibrations, they can be assigned to the peaks at 860–864 and 816–822 cm^{-1}, respectively. Deformation vibrations at 681–685, 629–633 and 596 cm^{-1} can be assigned to the bending of the BO_3 groups and peaks observed in the region of 562–567 and 491–493 cm^{-1} are attributed to the bending mode of BO_4 groups.[33]

The materials can absorb UV light with wavelength around 320 nm (Fig. 2(a) and (b)). The band gap energy of KBB and KBC are obtained by $(\alpha h\nu)^2$ plotted against $h\nu$ as shown in the plates. The position of the valence band (VB) and conduction band (CB) of the semiconductor can be further estimated according to the following eqn (1) and (2):[34,35]

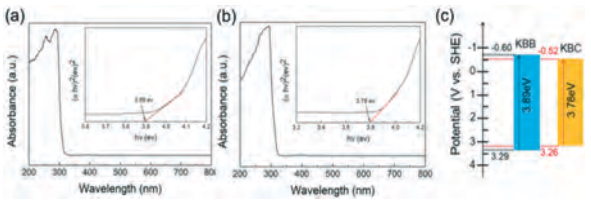

Fig. 2 UV-vis diffuse reflectance spectrum (a) and (b) for KBB and KBC, and inset of (a) and (b): the plots are the curves of $(\alpha h\nu)^2$ *vs.* $h\nu$ for the samples; (c) band structures of KBX samples.

$$E_{VB} = X - E_e + 0.5E_g \quad (1)$$

$$E_{CB} = E_{VB} - E_g \quad (2)$$

where E_{VB} and E_{CB} are the VB and CB potential of the semiconductor, respectively; X is the electronegativity of the material, which is obtained by calculating the absolute electronegativity of the constituent atoms (X_K = 2.7882 eV, X_B = 4.5951 eV, X_O = 8.3703 eV, X_{Br} = 6.4079, X_{Cl} = 6.8446). E_e is the hydrogen standard potential for free electrons (~4.5 eV). The Mott–Schottky tests were used to estimate the positions of conduction band (CB). As shown in Fig. S4,† the flat potentials of KBB and KBC are located at −1.20 and −1.13 V (*vs.* SCE), which respectively corresponds to −0.59 and 0.52 V (*vs.* SHE). Fig. 2(c) shows the band structures of KBX. The exact calculation results were shown in Table S2.† It is indeed that the optical properties of the crystals were influenced by the halogen atoms substitution.

Photocatalytic activity and PEC analysis

The photocatalytic activity of KBX were tested by measuring the dechlorination of CPs (2-CP, 2,4-DCP, 2,4,6-TCP) under UV light irradiation. It can be seen in Fig. 3(a) more than 92.0% of the 2-CP was degraded within 16 min and the ultimate degradation ratio was 92.2% and 97.6% for KBB and KBC, respectively. The P25 TiO_2 was used as reference and only about 43.0% of 2-CP was degraded under the same

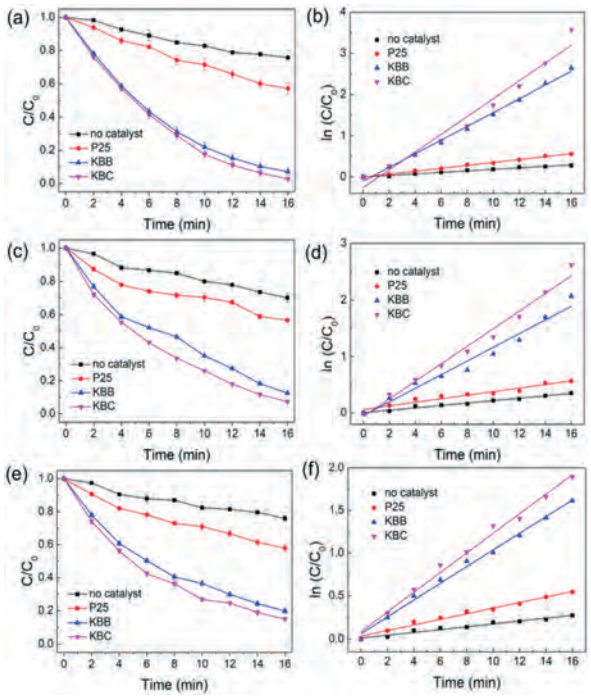

Fig. 3 Photo-dechlorination (a), (c) and (e) of 2-CP, 2,4-DCP and 2,4,6-TCP in aqueous dispersions over samples of KBB and KBC under UV light irradiation; the pseudo first-order kinetic fitting linear simulation curves (b), (d) and (f) for the photodegradation of CPs over the prepared photocatalysts.

conditions. The blank test was also taken, about 24.4% of 2-CP degradation could be observed. Photocatalytic reaction results with other CPs (2,4-DCP and 2,4,6-TCP) were shown in Fig. 3(c) and (e). The degradation of CPs by KBC was found to be faster than that of KBB, suggesting KBC has a better photocatalytic activity. According to the photocatalytic activity of photocatalytic degradation of 2-CP, 2,4-DCP and 2,4,6-TCP by KBB or KBC, the rate of photocatalytic degradation decreased with the increase of the number of chlorophenol substituents. It can be seen that the dechlorination pathway of chlorophenol is related to the number of chlorine atoms and the position on the benzene ring.[36,37] The more the number of chlorine substituents, the more toxic the pollutants are and the more difficult it is to degrade.

As shown in Fig. 3(b), (d) and (f), the degradation data was well fitted by the pseudo-first-order kinetics equation as follows:

$$d[C]/dt = -k[C] \quad (3)$$

where $[C]$ is the concentration of the aqueous solution of CPs, t is the reaction time, and k is the pseudo-first-order rate constant. The rate constant k can be obtained from a linear fit curve of ln ($[C]t/[C]0$) to t. The degradation performances of P25 TiO_2 and KBX photocatalysts over the CPs systems were compared in Table 1. The rate constant for photocatalytic dechlorination of 2-CP using KBB and KBC were 0.1667 and 0.2159 min^{-1}, respectively, which was nearly 6 times faster than that of commercial P25 TiO_2 catalyst (0.0355 min^{-1}). This clearly shows that KBX had an excellent photocatalytic activity for dechlorination of CPs. The BET specific surface area of KBB and KBC samples were 5.2 and 5.6 $m^2\ g^{-1}$, respectively, which means that the high photocatalytic activity of KBX materials was almost unaffected by the specific surface area (Fig. S5†). The stability of photocatalyst was further performed and the specific discussion was shown in ESI† (Fig. S6).

To further confirm the proposed photocatalytic activity, a combined analysis of PEC including transient photocurrent response (TPC) and electrochemical impedance spectroscopy (EIS) were performed. Rapid generation of photocurrent and excellent reproducibility occur when the KBX samples irradiated under UV light as shown in Fig. S7(a).† When the bias potential was 0 V, the anode photocurrent intensity of KBC was higher than that of KBB (Fig. S7(a)†), suggesting that the recombination efficiency of photo-generated carriers was reduced compared with KBB during the photoreaction, which was consistent with the photocatalytic activity analysis. EIS analysis was used to explore the charge transport of photocatalyst and composite materials. The arc radius of KBC was smaller than that of KBB, which proves that KBC has smaller electric resistance of the electrode and the higher efficiency of charge separation as shown in Fig. S7(b).† Moreover, the solid powder fluorescence tests of KBB and KBC samples are conducted to explore the recombination of photo-generated electrons and holes. As shown in Fig. S7(c),† KBC exhibits lower fluorescence intensity, indicating the recombination efficiency of the photo-generated electrons and holes lower than that of KBB, which is consistent with the result of the photocatalytic degradation of CPs.

Table 1 The rate constants (k), correlation coefficient r^2 and degradation efficiency (%) for CPs (2-CP, 2,4-DCP, 2,4,6-TCP) dechlorination over KBX and P25 samples

		No catalyst	P25	KBB	KBC
2-CP	k (min^{-1})	0.0185	0.0355	0.1667	0.2159
	r^2	0.9818	0.9953	0.9949	0.9661
	Degradation efficiency (%)	24.4	43.0	92.2	97.9
2,4-DCP	k (min^{-1})	0.0214	0.0316	0.1208	0.1555
	r^2	0.9811	0.9373	0.9674	0.9830
	Degradation efficiency (%)	29.8	43.3	87.1	92.8
2,4,6-TCP	k (min^{-1})	0.0165	0.0322	0.0975	0.1148
	r^2	0.9686	0.9829	0.9933	0.9898
	Degradation efficiency (%)	24.2	42.1	80.1	85.1

Distortion calculation and internal electric field

From the above experiment we clearly see that, although the KBC and KBB samples have the same crystal structure, the photocatalytic properties of KBC is obviously superior to KBB. Therefore, the construction of each material was deeply investigated, it is commonly considered that Cl atom performs a more electronegativity than Br atom thus the nonconcentric properties of each material will produce a different second harmonic generation (SHG) response. In order to distinguish the internal electric field strengths of the two polar materials of KBB and KBC, the second harmonic generation (SHG) measurement is performed on KBX which is an effective method for indicating the electric field strength inside the polar material.[38] The experiment detail has been described in in the Supplementary Information 1.4 and the curve result is shown in Fig. S8.† It can be seen that the KBC has a higher SHG intensity than that of KBB, which is approximately 1.8 and 2.7 times, respectively, of the KDP standard when using same particle size, indicating that the internal polarization ability of KBC is superior to KBB. Obviously, as the particle size increases, the SHG intensity of KBX shows an increased trend. Thus, the distortion ability of KBC in present is stronger than KBB. Furthermore, to further support the above deduction, the out-of-center distortions of XK_6 (X = Cl, Br) octahedrons controlled by the size of X atoms and its coordination environment were carefully studied. When X atom in the XM_6 octahedrons is different, the tilting or twisting will be produced and the out-of-center distortion will also happens to change. The XK_6 octahedrons are distorted along the C_3 direction (Fig. 4). Usually, the magnitude of the out-of-center distortion (Δd) related to the electronegativity of the halogen atoms.[39] When Δd = 0.00–0.05, the structure is preferred to have no or very weak distortion, while, when Δd equal to 0.05–0.40, the weak distortion will

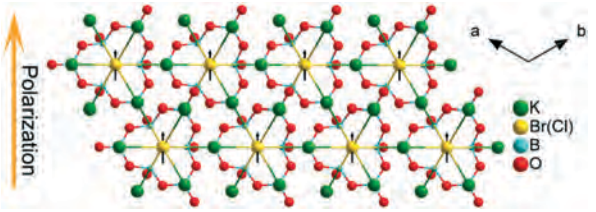

Fig. 4 Ball-and-stick diagrams of KBX structures and the direction of electric polarization is indicated by the arrow along the *c*-axis.

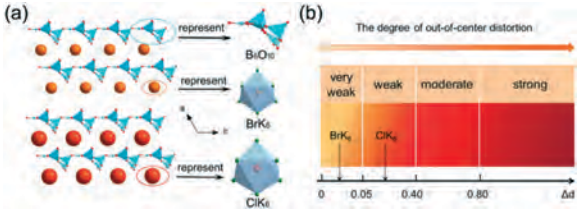

Fig. 5 (a) The KBX structures of non-centrosymmetric polar materials is composed of B_6O_{10} (blue oval circle) and BrK_6 (Orange oval circle) or ClK_6 (red oval circle) units, respectively. (b) Different degrees of out-of-center distortions correspond to different values of Δd.

happen. The octahedral distortion Δd parameters in XK_6 octahedrons are defined as:

$$\Delta d = \frac{\left|(\text{X–K1}) - (\text{X–K4})\right|}{\left|\cos\theta_1\right|} + \frac{\left|(\text{X–K2}) - (\text{X–K5})\right|}{\left|\cos\theta_2\right|} + \frac{\left|(\text{X–K3}) - (\text{X–K6})\right|}{\left|\cos\theta_3\right|}$$

where the pairs (K1, K4), (K2, K5), and (K3, K6) are the atoms forming an octahedron and located in positions opposite to each other; and these *trans* bond angles are as follows:

$$\theta_1 = \angle\text{K1–X–K4}$$

$$\theta_2 = \angle\text{K2–X–K5}$$

$$\theta_3 = \angle\text{K3–X–K6}$$

Accordingly, the Δd values of XK_6 octahedrons in the crystal structures were calculated to be 0.137 (KBC) and 0.027 (KBB). Therefore, the out-of-center distortion of the BrK_6 octahedron was smaller than that of the ClK_6 octahedron.[40] This phenomenon was further confirmed by analyzing the changes of diffraction peaks in XRD pattern of two samples. For the KBX sample, a slight shift towards the higher 2θ of the corresponding diffraction peaks can be observed with the replacement of different halogen atoms, as shown by the peak at (211) at higher magnification in Fig. S9.† This observation clearly shows that the interplanar spacing changes and the lattice distortion of each material are different.

In general, the internal electric field exists in the polar structure of KBX with nonconcentric symmetry, indicating that the spontaneous polarization largely determines its special photocatalytic properties.[41] Fig. 5(a) depicts the polar structure of the KBX crystals. When the halide atoms are displaced from the center of the XK_6 octahedrons, the out-of-center distortion is nonzero value; while the distortion will be zero when the ligands move in the equal and opposite directions.[37] The local coordinated environment of Br and Cl atoms reveals the occurrence of distortion along the *c*-axis of the polar axis with some degrees of polar displacements of 0.027 and 0.137 along this direction, leading to a distorted polyhedron. The distorted XK_6 octahedrons may cause changes in the internal electric field and further influence the photocatalytic activity of polar materials. According to the fact that different out-of-center distortions will influence the holes or electrons drifts under light excitation. Therefore, a slightly larger distortion of KBC than that of KBB may be due to the larger electronegativity of Cl atom (Fig. 5(b)).[42]

The surface potential can be detected by AFM combined with KPFM method which were used to analyze the light-induced charge transfer properties, the built-in electric field effect, and the difference in surface potential (SP) on the materials before and after illumination.[43] Fig. 6(a)/(a′) and (c)/(c′) show the AFM images of KBX material in dark and under irradiation. As seen from the figure, the morphology of the sample does not change before and after illumination, indicating that the morphology of the material was not influenced by light. As shown in Fig. 6(b)/(b′), (d)/(d′) and (e)/(e′), SP of samples may change after irradiation, corresponding to the dark (red line) and light (blue line) conditions. The average value of the SP changes in the dark along the line AB was 9.82 and 7.86 mV, and the SP significantly shifted down to 5.11 and −4.74 mV (line A′B′) under illumination. Therefore, the average SP of both phases were reduced by about 4.71 and 12.6 mV for KBB (Fig. 6(e)) and KBC (Fig. 6(e′)), respectively. This should be due to the band bending induced by the surface state and charge during the light excitation. Compared to KBB, the ΔCPD change of KBC shows a large negative shift of −12.6 mV, demonstrating that the electric field inside the polarized materials can provide the driving force for photoelectrons and holes, between the C^+ and C^- domains. The separation of photo-generated carriers at the interface will also lead to the accumulation of electrons and holes in different regions, thus causing a potential difference at the surface of the material.[44]

Roles of active species and possible photocatalytic mechanism

Active species are vital to the photocatalyst process. In the experiment, we tried a series of trapping agent to determine the presence of the active species. DMPO is a typical spin trapping

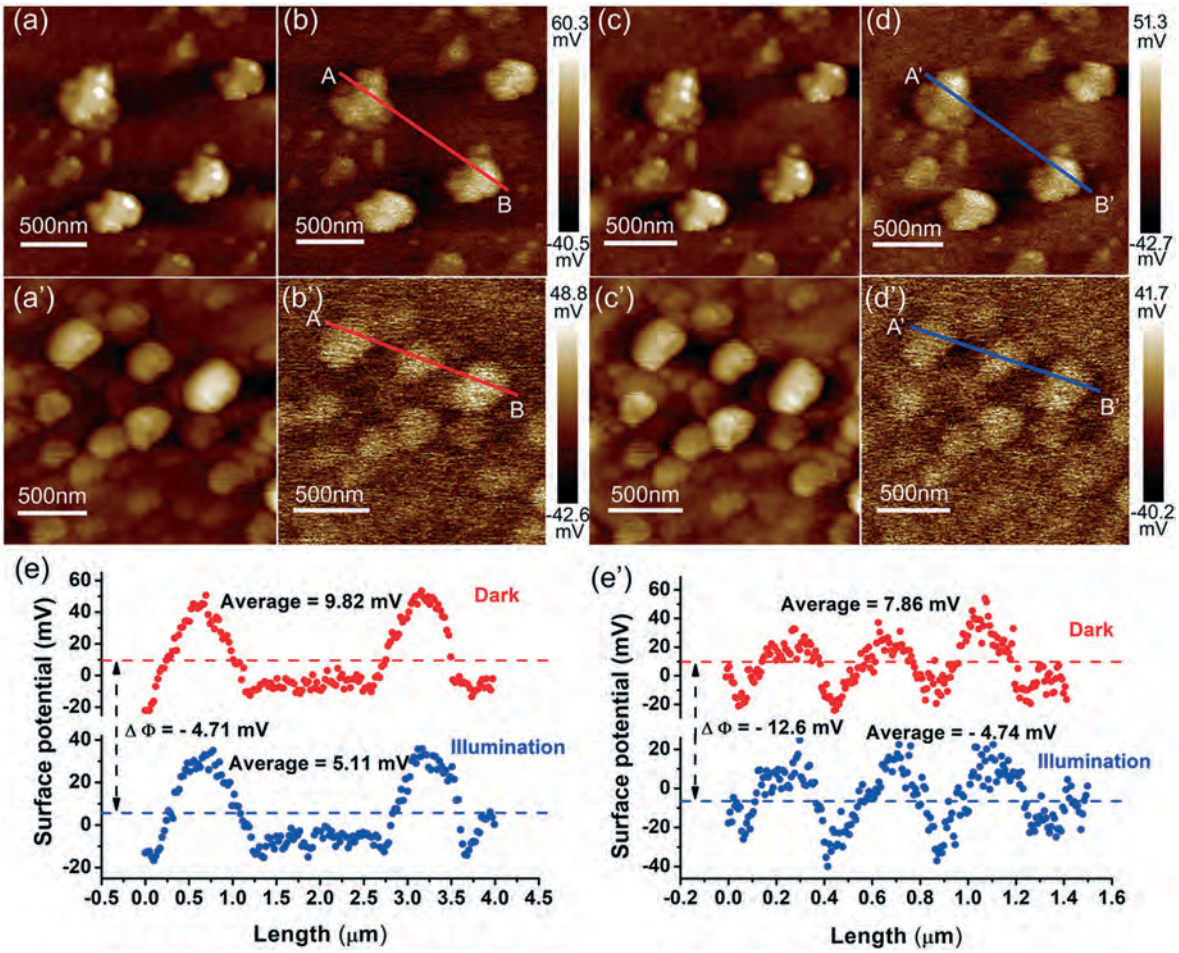

Fig. 6 AFM topographic images and KPFM phase images in the dark (a)/(a′) and (b)/(b′) and under illumination (c)/(c′) and (d)/(d′); (e)/(e′) surface potential profile along the red line in the inset of (b)/(b′) measured in the dark and the blue line in the inset of (d)/(d′) measured under illumination for the KBB and KBC, respectively.

agent for trapping $^{\bullet}O_2^-$ and $^{\bullet}OH$ radicals.[45] In the absence of light, no significant $^{\bullet}O_2^-$ specific peaks were produced in the samples. As shown in Fig. 7(a) and (b), after 2 min of light irradiation, the ESR signal from $^{\bullet}O_2^-$ was detected, and the intensity of the characteristic peak of $^{\bullet}O_2^-$ evenly increased after 6 min, indicating that the samples KBX can produce more $^{\bullet}O_2^-$ substances under long-time illumination.

Fig. 7(c) and (d) shows the change in ESR intensity that generates $^{\bullet}OH$ free radicals after light irradiation of an aqueous solution containing KBX for 30, 60 and 90s. Four fold signals from the DMPO–OH adduct relative intensity of 1 : 2 : 2 : 1 were clearly observed during the test, indicating that $^{\bullet}OH$ radicals will be formed in the photocatalytic reaction. With the increase of the illumination time, the signal intensity of the ESR adducts of different reactive species (RSs) increased, indicating that the RSs increased in the reactions, and thus the target pollutant could be degraded.

Photo-generated electrons were confirmed by TEMPO method, which is a typical spin label molecule with a stable triplet ESR spectrum. When it reacts with electrons, the ESR signal of TEMPO will be reduced, as the TEMP-OH produced the ESR signal will be disappeared.[46] Fig. 7(e) and (f) shows the electronic ESR signal changes in the suspension containing KBX samples. The ESR spectrum of the TEMPO aqueous solution shows a stable signal with three peaks of intensity 1 : 1 : 1. In the presence of KBX, there was a slight decrease of the signal intensity within 30s irradiation. After 120 s of irradiation, there was a considerable decrease in ESR signal. As time goes on, KBX have more reductions, indicating that photo-excited electrons were generated.

To determine role of each RSs of KBX (X = Br, Cl) photocatalysts in the photocatalytic reaction processes, different scavenger agents were used in the degradation of 2-CP. In this study, *p*-BQ, $AgNO_3$, TBA, and KI were respectively used as superoxide radical ($^{\bullet}O_2^-$), electron (e^-), hydroxyl radicals ($^{\bullet}OH$), and holes (h^+) scavengers.[47,48] To clarify the contribution role of the different RSs, the two materials were compared as shown in Fig. 8(a). The activity tests of RSs capture experiments for 2-CP degradation over time were shown in Fig. 8(b) and (c), and the first order rate constants were listed in Table 2. When there was no scavenger, the degradation efficiency was 97.9% and the rate constant was 0.2159 min^{-1}.

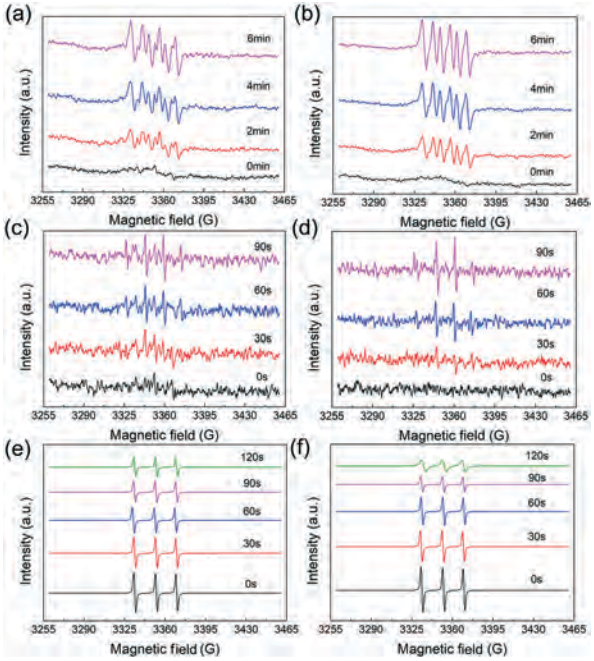

Fig. 7 Different signal intensity peaks of ESR adducts for (a) and (b) $^{\cdot}O_2^-$; (c) and (d) $^{\cdot}OH$; (e) and (f) e^- over different illumination time of KBB and KBC samples in aqueous dispersion under UV light irradiation.

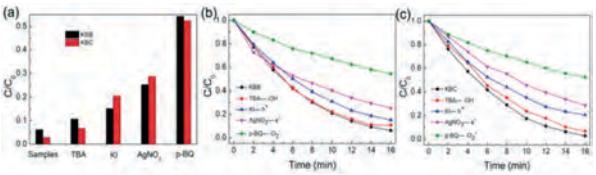

Fig. 8 (a) Photocatalytic degradation of 2-CP over KBB and KBC samples under UV light irradiation in the presence of different scavengers; reactive species trapping studies of 2-CP degradation activity with the addition of different scavengers under UV light irradiation over samples (b) KBB and (c) KBC.

Table 2 The rate constants and contribution rates for photocatalytic degradation of 2-CP with the addition of different scavengers, [KBC] = 0.05 g L^{-1}

Photocatalytic conditions	Quenching RSs	Scavenger concentration (mmol L^{-1})	k (min^{-1})	Contribution rate/%
No scavengers	—	—	0.2159	—
TBA	Quench $^{\cdot}OH$	50	0.1982	8.2
		100	0.1679	22.2
KI	Quench h^+	50	0.1308	39.4
		100	0.1021	52.7
$AgNO_3$	Quench e^-	20	0.1032	52.2
		50	0.0780	63.9
P-BQ	Quench $^{\cdot}O_2^-$	0.5	0.0651	69.9
		1	0.0396	81.7

After the addition of *p*-BQ, the degradation was strongly inhibited due to the scavenging of $^{\cdot}O_2^-$ radicals, and its degradation efficiency was 47.6%. The introduction of $AgNO_3$ also significantly reduced the degradation efficiency (71.5%) and the average rate constant (0.0780 min^{-1}). Similarly, the degradation of 2-CP was also inhibited to a certain extent when KI and TBA were added to the reaction system. The degradation efficiency was 79.0% and 93.2%, respectively. Therefore, the role of different reactive species on the degradation of 2-CP in the order of $^{\cdot}O_2^- > e^- > h^+ > {}^{\cdot}OH$.

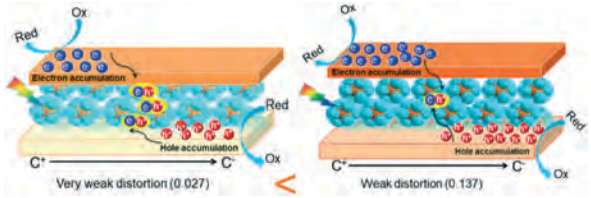

Scheme 1 Scheme showing the internal polarization field of non-centrosymmetric polar materials KBX enhances charge separation and photocatalytic mechanism.

The intermediate product of photocatalytic degradation of 2-CP was identified by LC–MS method, as shown in Fig. S10 and Table S3.† Compounds such as 2-chloro-hydroquinone, 2-chloro-5-hydroxyoyclohexa-benzoquinone, 2-hydroxy-1.4-benzoquinone and phenol are the main intermediates formed during photocatalytic degradation of 2-CP. Based on the experimental results of the study, the pathway for 2-CP photocatalytic degradation is proposed in Fig. S11.† From the LC-MS result, we can clearly see that although 2-CP cannot be completely dechlorinated by KBC, the degradation intermediates and final products are less toxic than 2-CP and can be easily biodegraded into harmless compounds by microorganisms under both aerobic and anaerobic conditions.[3,49]

From the above experiments, the possible mechanisms for the photocatalyst activity of each sample was deduced as followings, the effective separation of photo-generated electrons-holes pairs in KBX materials can result in the rapid transfer of interfacial charges, which is mainly affected by out-of-center distortion. As shown in Scheme 1, the Cl ion has a greater electronegativity than Br, which attracts more electrons and repels holes on the surface of the materials. The accumulation of surface electrons to form more active free radicals and can fully degrade the target contaminants into harmless or less harmful products. Moreover, the out-of-center distortions of the XK_6 octahedrons in the KBX crystal structures can cause an internal electric field with spontaneous polarization. The resulting charged surface causes the photo-generated carriers to move in the opposite direction, and the polarized materials with large spontaneous polarization generate larger driving forces to separate photo-generated carriers.

Conclusions

Overall, two different halogen-substituted $K_3B_6O_{10}X$ (X = Cl, Br) materials were obtained by a simple conventional high-temperature solid-phase method. The crystal structure, micro-morphology, photo-dechlorination performance, the

role of RSs in the process, and the effect of X atoms substitution for the out-of-center distortions of the materials were systematically explored. The photocatalytic dechlorination activity shows a good correlation with the coordination environment of halide X atoms in XM_6 (X = Cl, Br) octahedrons. We believe that a larger polarization capacity of the material gives rise to a larger built-in electric field within the space charge region. Next, we will explore some methods to modify the material of the system to broaden the spectral response range and focus on the more systematic effects of different halogen atoms or alkali metal cations on the structure and properties of $M_3B_6O_{10}X$ (M = alkali metal; X = Cl, Br) systems.

Conflicts of interest

There are no conflicts to declare.

Acknowledgements

This work was supported by the National Natural Science Foundation of China (51772325), and Natural Science Foundation of Xinjiang Uygur Autonomous Region (2016D01A072).

Notes and references

1 L. Wang, D. Kong, Y. Ji, J. Lu, X. Yin and Q. Zhou, *Chem. Eng. J.*, 2018, **343**, 235–243.
2 W. Q. Li, Z. H. Wen, S. H. Tian, L. J. Shan and Y. Xiong, *Catal. Sci. Technol.*, 2018, **8**, 1051–1061.
3 N. Yang, J. Cui, L. Zhang, W. Xiao, N. A. Akram and X. Mao, *J. Chem. Technol. Biotechnol.*, 2015, **91**, 938–947.
4 H. Jia, G. Nulaji, H. Gao, F. Wang, Y. Zhu and C. Wang, *Environ. Sci. Technol.*, 2016, **50**, 6310–6319.
5 S. J. Ki, K.-J. Jeon, Y.-K. Park, S. Jeong, H. Lee and S.-C. Jung, *Catal. Today*, 2017, **293-294**, 15–22.
6 M. Á. Arellano-González, I. González and A.-C. Texier, *J. Hazard. Mater.*, 2016, **314**, 181–187.
7 W. Q. Li, Z. H. Wen, S. H. Tian, L. J. Shan and Y. Xiong, *Catal. Sci. Technol.*, 2018, **8**, 1051–1061.
8 L. Ren, J. Zhang, Y. Li and C. Zhang, *Chem. Eng. J.*, 2011, **168**, 553–561.
9 F. Li, P. Du, W. Liu, X. Li, H. Ji, J. Duan and D. Zhao, *Chem. Eng. J.*, 2018, **331**, 685–694.
10 Z. Lian, W. Wang, G. Li, F. Tian, K. S. Schanze and H. Li, *ACS Appl. Mater. Interfaces*, 2017, **9**, 16959–16966.
11 L. Liu, F. Chen, F. Yang, Y. Chen and J. Crittenden, *Chem. Eng. J.*, 2012, **181–182**, 189–195.
12 Z. Kam, X. Wang, J. Zhang and J. Wu, *ACS Appl. Mater. Interfaces*, 2015, **7**, 1608–1615.
13 H. Lachheb, F. Ajala, A. Hamrouni, A. Houas, F. Parrino and L. Palmisano, *Catal. Sci. Technol.*, 2017, **7**, 4041–4047.
14 H. Anwer and J.-W. Park, *J. Hazard. Mater.*, 2018, **358**, 416–426.
15 J. Yang, R. Hu, W. Meng and Y. Du, *Chem. Commun.*, 2016, **52**, 2620–2623.
16 L. Yang, J. Huang, L. Shi, L. Cao, Q. Yu, Y. Jie, J. Fei, H. Ouyang and J. Ye, *Appl. Catal., B*, 2017, **204**, 335–345.
17 F. t. Li, S. j. Liu, Y. b. Xue, X. j. Wang, Y. j. Hao, J. Zhao, R. h. Liu and D. Zhao, *Chem. – Eur. J.*, 2015, **21**, 10149–10159.
18 H. Li, Y. Gao, Y. Zhou, F. Fan, Q. Han, Q. Xu, X. Wang, M. Xiao, C. Li and Z. Zou, *Nano Lett.*, 2016, **16**, 5547–5552.
19 H.-R. Wang, G.-Y. Zhang, Y.-Y. Xu, X.-M. Wei, X.-Q. Shen and Y.-Q. Sun, *CrystEngComm*, 2016, **18**, 8089–8100.
20 H. Shi, J. Chen, G. Li, X. Nie, H. Zhao, P.-K. Wong and T. An, *ACS Appl. Mater. Interfaces*, 2013, **5**, 6959–6967.
21 J. Schneider, M. Matsuoka, M. Takeuchi, J. Zhang, Y. Horiuchi, M. Anpo and D. W. Bahnemann, *Chem. Rev.*, 2014, **114**, 9919–9986.
22 L. Li, P. A. Salvador and G. S. Rohrer, *Nanoscale*, 2014, **6**, 24–42.
23 J. Liu, X. Fan, Y. Zhu, J. Zhao, F. Jiang, S. Chen, H. Sun, J. Xu, W. Deng and C. Wang, *Appl. Catal., B*, 2016, **181**, 436–444.
24 X. Fan, Z. Wu, L. Wang and C. Wang, *Chem. Mater.*, 2017, **29**, 639–647.
25 J. Jiang, K. Zhao, X. Xiao and L. Zhang, *J. Am. Chem. Soc.*, 2012, **134**, 4473–4476.
26 B. Zhang, Z. Wang, B. Huang, X. Zhang, X. Qin, H. Li, Y. Dai and Y. Li, *Chem. Mater.*, 2016, **28**, 6613–6620.
27 H. Huang, X. Li, J. Wang, F. Dong, P. K. Chu, T. Zhang and Y. Zhang, *ACS Catal.*, 2015, **5**, 4094–4103.
28 K. Wu, Z. Yang and S. Pan, *Angew. Chem., Int. Ed.*, 2016, **55**, 6713–6715.
29 Y. Wang and S. Pan, *Coord. Chem. Rev.*, 2016, **323**, 15–35.
30 H. Yu, H. Wu, S. Pan, Z. Yang, X. Hou, X. Su, Q. Jing, K. R. Poeppelmeier and J. M. Rondinelli, *J. Am. Chem. Soc.*, 2014, **136**, 1264–1267.
31 A. G. Al-Ama, E. L. Belokoneva, S. Y. Stefanovich, O. V. Dimitrova and N. N. Mochenova, *Crystallogr. Rep.*, 2006, **51**, 225–230.
32 H. Wu, S. Pan, K. R. Poeppelmeier, H. Li, D. Jia, Z. Chen, X. Fan, Y. Yang, J. M. Rondinelli and H. Luo, *J. Am. Chem. Soc.*, 2011, **133**, 7786–7790.
33 Y. Wang, S. Pan, X. Tian, Z. Zhou, G. Liu, J. Wang and D. Jia, *Inorg. Chem.*, 2009, **48**, 7800–7804.
34 A. H. Nethercot, *Phys. Rev. Lett.*, 1974, **33**, 1088–1091.
35 Z. Jiang, Y. Liu, M. Li, T. Jing, B. Huang, X. Zhang, X. Qin and Y. Dai, *Sci. Rep.*, 2016, **6**, 22727.
36 W. Z. Tang and C. P. Huang, *Waste Manage.*, 1995, **15**, 615–622.
37 K. Hideyuki, K. Satoshi, S. Tohru, O. Kiyohisa and Y. Yoshihiro, *Chemosphere*, 2006, **63**, 592–599.
38 M. Zhang, S.-L. Pan, X.-Y. Fan, Z.-X. Zhou, K. R. Poeppelmeier and Y. Yang, *CrystEngComm*, 2011, **13**, 2899–2903.
39 P. S. Halasyamani, *Chem. Mater.*, 2004, **16**, 3586–3592.
40 C. Bai, H. Yu, S. Han, S. Pan, B. Zhang, Y. Wang, H. Wu and Z. Yang, *Inorg. Chem.*, 2014, **53**, 11213–11220.
41 W. Wang, B. Huang, X. Ma, Z. Wang, X. Qin, X. Zhang, Y. Dai and M.-H. Whangbo, *Chem. – Eur. J.*, 2013, **19**, 14777–14780.
42 H. W. Eng, P. W. Barnes, B. M. Auer and P. M. Woodward, *J. Solid State Chem.*, 2003, **175**, 94–109.
43 S. V. Kalinin, A. N. Morozovska, L. Q. Chen and B. J. Rodriguez, *Rep. Prog. Phys.*, 2010, **73**, 056502.

